On drag reduction scaling and sustainability bounds of superhydrophobic surfaces in high Reynolds number turbulent flows

Amirreza Rastegari[1] **and Rayhaneh Akhavan**[1,†]

[1]Department of Mechanical Engineering, The University of Michigan, Ann Arbor, MI 48109-2125, USA

The drag reduction characteristics and sustainability bounds of superhydrophobic (SH) surfaces in high Reynolds number turbulent flows are investigated using results from direct numerical simulation (DNS) and scaling-law analysis. The DNS studies were performed, using lattice Boltzmann methods, in turbulent channel flows at bulk Reynolds numbers of $Re_b = 3600$ ($Re_{\tau_0} \approx 222$) and $Re_b = 7860$ ($Re_{\tau_0} \approx 442$) with SH longitudinal microgrooves or SH aligned microposts on the walls. Surface microtexture geometrical parameters corresponding to microgroove widths or micropost spacings of $4 \lesssim g^{+0} \lesssim 128$ in base flow wall units and solid fractions of $1/64 \leqslant \phi_s \leqslant 1/2$ were investigated at interface protrusion angles of $\theta_p = 0°$ and $\theta_p = -30°$. Analysis of the governing equations and DNS results shows that the magnitude of drag reduction is not only a function of the geometry and size of the surface microtexture in wall units, but also the Reynolds number of the base flow. A Reynolds number independent measure of drag reduction can be constructed by parameterizing the magnitude of drag reduction in terms of the friction coefficient of the base flow and the shift, $(B - B_0)$, in the intercept of a logarithmic law representation of the mean velocity profile in the flow with SH walls compared to the base flow, where $(B - B_0)$ is Reynolds number independent. The scaling laws for $(B - B_0)$, in terms of the geometrical parameters of the surface microtexture in wall units, are presented for SH longitudinal microgrooves and aligned microposts. The same scaling laws are found to also apply to liquid-infused (LI) surfaces as long as the viscosity ratios are large, $N \equiv \mu_o/\mu_i \gtrsim 10$. These scaling laws, in conjunction with the parametrization of drag reduction in terms of $(B - B_0)$, allow for *a priori* prediction of the magnitude of drag reduction with SH or LI surfaces in turbulent flow at any Reynolds number. For the most stable of these SH surface microtextures, namely, longitudinal microgrooves, the pressure stability bounds of the SH surface under the pressure loads of turbulent flow are investigated. It is shown that the pressure stability bounds of SH surfaces are also significantly curtailed with increasing Reynolds number of the flow. Using these scaling laws, the narrow range of SH surface geometrical parameters which can yield large drag reduction as well as sustainability in high Reynolds number turbulent flows is identified.

Key words: drag reduction, turbulence control

† Email address for correspondence: raa@umich.edu

1. Introduction

Superhydrophobic (SH) surfaces have received much attention as a means of skin-friction drag reduction in wall-bounded turbulent flows in recent years (Rothstein 2010). These are surfaces with apparent receding contact angle exceeding a certain value, e.g. 150° (Schellenberger *et al.* 2016), which repel liquids by trapping gas inside the nano- or micro-scale features of a textured hydrophobic surface. The entrapped gas prevents direct contact between the liquid and the wall, leading to the so-called Cassie–Baxter state, and providing a mechanism for liquid slip at the wall. This effective slip has been shown to be the primary mechanism of skin-friction drag reduction with SH surfaces in both the laminar and turbulent flow regimes (Rastegari & Akhavan 2015, 2018*a*).

Drag reductions of up to 50 % (Daniello, Waterhouse & Rothstein 2009) and up to 75 % (Park, Sun & Kim 2014) have been reported in laboratory-scale experiments in turbulent channel flows and turbulent boundary layer flows, at $135 \lesssim Re_{\tau_0} \lesssim 250$, using SH longitudinal microgrooves with solid fractions of $\phi_s = 0.5$ and $\phi_s = 0.05$, respectively, where $Re_{\tau_0} \equiv u_{\tau_0} \delta / \nu$ is the friction Reynolds number in the base flow, u_{τ_0} is the wall friction velocity in the base flow, δ is the boundary layer thickness or channel half-height and ν is the kinematic viscosity. It has been noted that the magnitude of drag reduction increases with increasing width of the surface microtexture indentations, g, and decreasing solid fraction, ϕ_s, approaching a maximum drag reduction of $DR \sim (1 - \phi_s)$ in the limit of large g (Daniello *et al.* 2009; Rothstein 2010; Park, Park & Kim 2013). Scaling laws have been proposed for the slip length and the slip velocity in terms of g and ϕ_s in both the laminar (Ybert *et al.* 2007) and turbulent (Seo & Mani 2016) flow regimes. However, the relation between these scaling laws and the magnitude of drag reduction has not been clarified.

These drag reduction capabilities of SH surfaces, however, are lost if the SH surface undergoes a wetting transition, from the Cassie–Baxter state to a Wenzel state, whereby the trapped gas pockets inside the surface microtexture are depleted and replaced with the working fluid. This wetting transition can occur because of (i) depinning of the contact line and/or sagging of the liquid–gas interface under high local pressures (Zheng, Yu & Zhao 2005; Checco *et al.* 2014) or (ii) diffusion or entrainment of the gas layer into the working liquid under high local shear rates (Samaha, Tafreshi & Gad-el Hak 2012; Karatay, Tsai & Lammertink 2013; Wexler, Jacobi & Stone 2015; Ling *et al.* 2017) of turbulent flow.

There is also anecdotal evidence, from both direct numerical simulation (DNS) and experiments, which suggests that, for a given geometry and size of the surface microtexture in wall units, the drag reduction performance of SH surfaces degrades with increasing Reynolds number of the base flow (Rastegari & Akhavan 2018*a*). Here, and throughout this study, 'wall units' refers to normalization with respect to the wall friction velocity of the drag reduced flow, u_τ, and the kinematic viscosity, ν, and quantities normalized in this manner are denoted by a $+$ superscript. This degradation in drag reduction has been recently demonstrated in DNS studies of turbulent channel flows with SH longitudinal microgrooves at $Re_{\tau_0} \approx 222$ and 442 (Rastegari & Akhavan 2018*a*), and can also be observed in earlier DNS studies of turbulent channel flows with SH longitudinal microgrooves at $180 \lesssim Re_{\tau_0} \lesssim 590$ (Park *et al.* 2013, figure 8b), even though the authors do not comment on it. Evidence of this degradation in drag reduction can also be found in recent experimental studies in turbulent boundary layer flows with spray coated SH walls, where a given upwards shift of the logarithmic layer in wall units, corresponding to $\Delta U^+ = 1.1$, was found

to result in 12 % drag reduction at $Re_{\tau_0} \approx 863$, but only 11 % drag reduction at $Re_{\tau_0} \approx 1408$ (Ling *et al.* 2016).

While other experimental studies have reported an enhancement of drag reduction with increasing Reynolds number in SH turbulent boundary layer flows (Zhang *et al.* 2015) or in SH or liquid-infused (LI) turbulent Taylor–Couette flows (Srinivasan *et al.* 2015; Van Buren & Smits 2017), it should be noted that these experiments were not performed with a fixed size of the surface microtexture in wall units at different Reynolds numbers. Instead, they used a given surface microtexture with a fixed size in 'physical units' at different Reynolds numbers, which leads to an increase in the size of the surface microtexture in wall units as the Reynolds number increases. As will be discussed in detail in §§ 3 and 4, an increase in the size of the surface microtexture in wall units can affect the drag reduction in a number of conflicting and competing ways. In the absence of a wetting transition or roughness effects, an increase in the size of the surface microtexture in wall units enhances the magnitude of drag reduction. However, an increase in the size of the surface microtexture in wall units also makes the surface more susceptible to a wetting transition, at which point the surface microtexture can begin to act as surface roughness and cause a drag increase. In addition, for random surface microtextures, where the height of the surface micro-features is variable, the protrusion heights of the surface elements above the liquid/gas interface will increase in wall units as the Reynolds number increases. This can also give rise to roughness effects with increasing Reynolds number, which can degrade the drag reduction. The interplay between these competing effects determines the trends in drag reduction when a surface microtexture of a given size in physical units is employed at different Reynolds numbers. Depending on which features are at play or dominate, the magnitude of drag reduction can be enhanced with increasing Reynolds number (Srinivasan *et al.* 2015; Zhang *et al.* 2015; Van Buren & Smits 2017), or degrade (Bidkar *et al.* 2014; Ling *et al.* 2016; Reholon & Ghaemi 2018), or show enhancement at low Reynolds numbers followed by degradation at higher Reynolds numbers (Aljallis *et al.* 2013; Bidkar *et al.* 2014; Gose *et al.* 2018). Collectively, the available experimental data in high Reynolds number SH turbulent boundary layer flows or SH turbulent channel flows, performed with a fixed size of the surface microtexture in physical units, show a trend towards enhancement of drag reduction with increasing Reynolds number up to a maximum of ∼30 % drag reduction at $Re_{\tau_0} \approx 1500$ (Aljallis *et al.* 2013; Zhang *et al.* 2015; Ling *et al.* 2016), followed by degradation of drag reduction at higher Reynolds numbers, approaching negative drag reductions at $Re_{\tau_0} \gtrsim 5000$ (Aljallis *et al.* 2013; Ling *et al.* 2016). These results all point to the need for an understanding of the scaling of drag reduction and the sustainability bounds of SH and LI surfaces with surface microtexture and flow parameters in turbulent flow.

The degradation in the drag reduction performance of microtextured surfaces with increasing Reynolds number of the base flow, for a fixed geometry and size of the surface microtexture in wall units, is a well-known feature of riblets (Bechert *et al.* 1997; Spalart & McLean 2011), where the highest drag reductions achieved in high Reynolds number turbulent flows of practical interest, with optimal 'blade riblets' of spacing ∼15 wall units (Bechert *et al.* 1997), were found to be nearly half the highest drag reductions, of ∼10 %, obtained with the same geometry and size of the riblets in wall units in laboratory-scale experiments (Spalart & McLean 2011). It has been suggested (Bechert *et al.* 1997; Spalart & McLean 2011; García-Mayoral & Jiménez 2012) that a Reynolds number independent measure of drag reduction can be constructed by parameterizing the magnitude of drag reduction in terms of the

friction coefficient of the base flow, C_{f_0}, and the shift, $(B - B_0)$, in the intercepts, B and B_0, of log-law representations of the normalized mean velocity profiles in the drag reduced and the base flow, respectively, where $(B - B_0)$ is Reynolds number independent and only a function of the geometry and size of the surface microtexture in wall units. In Rastegari & Akhavan (2018a), this formulation was extended to SH surfaces to obtain a parameterization of the magnitude of SH drag reduction in terms of C_{f_0} and the shift $(B - B_0)$.

While such a parametrization allows the drag reduction results from low Reynolds number turbulent flows to be extrapolated to higher Reynolds number flows of practical interest (Rastegari & Akhavan 2018a), developing optimal designs of SH surfaces also requires an understanding of the scaling laws for $(B - B_0)$ in terms of the geometrical parameters of the surface microtexture, as well as the sustainability bounds of SH surfaces in turbulent flow.

In this study, scaling arguments are combined with results from DNS of SH turbulent channel flows at $Re_{\tau_0} \approx 222$ and 442, performed with a wide range of SH longitudinal microgroove or aligned micropost surface microtexture geometrical parameters, to demonstrate the Reynolds number dependence of the drag reduction, and the Reynolds number independence of $(B - B_0)$, and to present the scaling laws for $(B - B_0)$ in turbulent flow in terms of the geometrical parameters of the SH surface in wall units. The combination of these parametrizations allow for *a priori* prediction of the magnitude of drag reduction with SH surfaces in turbulent flow at any Reynolds number. For the most stable of such SH surfaces, namely longitudinal microgrooves, we further present the pressure stability bounds of the SH surface in turbulent flow in terms of the Weber number, the geometrical parameters of the SH surface in wall units and the friction Reynolds number of the flow. These parameterizations are used to identify the narrow range of SH surface geometrical parameters which can ensure large drag reduction as well as sustainability in high Reynolds number turbulent flows of practical interest.

2. Numerical methods and simulation parameters

The DNS studies were performed in turbulent channel flows using standard D3Q19 (three-dimensional, 19 discrete velocity), single-relaxation-time lattice Boltzmann methods (Succi 2001) with grid embedding (Lagrava *et al.* 2012), of grid ratio 4 : 1, in the near-wall regions to better resolve the flow features near the SH walls. The resulting grid spacings were $\Delta_f^{+0} \approx 0.5$ for $z^{+0} \lesssim 30$, and $\Delta_c^{+0} \approx 2$ for $z^{+0} \gtrsim 30$ in all three directions in all the simulations, where Δ_f and Δ_c denote the grid spacings on the fine grid and the coarse grid, respectively, and the $+0$ superscript denotes normalization with respect to the kinematic viscosity, ν, and the wall-friction velocity, u_{τ_0}, of a 'base' turbulent channel flow with smooth, no-slip walls at the same bulk Reynolds number as the channel flow with SH walls. To preserve the order of accuracy of the lattice Boltzmann method, and ensure smoothness and continuity of the variables at the transition between the coarse and the fine grids, the two grids were overlapped for one cell width of the coarse grid, as suggested by Lagrava *et al.* (2012), and the interpolations between the two grids were performed using third-order bi-cubic Hermite splines in space, and second-order Hermite polynomials in time. The details of the numerical methods and verification studies performed to ensure the accuracy of the numerical methods and adequacy of the domain sizes and grid resolutions are described in the appendix of Rastegari & Akhavan (2018a).

The liquid/gas interfaces on SH walls were modelled as stationary, curved or flat shear-free boundaries, with the shape of the meniscus determined from an analytical
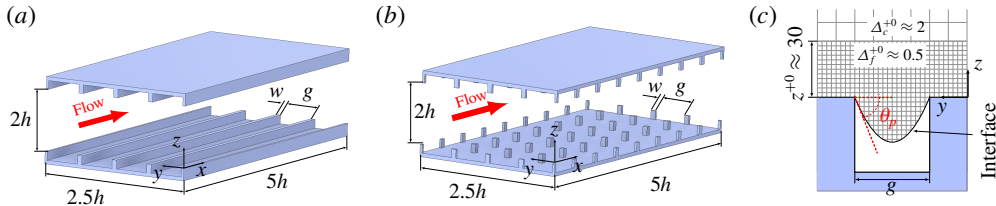
FIGURE 1. Schematic of the channels with SH walls, the coordinate system and the computational grid: (*a*) SH longitudinal microgrooves; (*b*) SH aligned microposts; (*c*) computational grid and protrusion angle.

solution of the Young–Laplace equation (Rastegari & Akhavan 2018*a*). Two interface protrusion angles of $\theta_p = 0°$ and $\theta_p = -30°$ were investigated, corresponding to liquid/gas interfaces which were either flat or at maximum advancing contact angle ($\theta_c = \theta_{F,adv} = 120°$), respectively.

The simulations were performed in channels of size $5h \times 2.5h \times 2h$ in the streamwise (x), spanwise (y) and wall-normal (z) directions, respectively, as shown in figure 1. A constant flow rate was maintained in the channel during the course of all simulations, corresponding to bulk Reynolds numbers of $Re_b \equiv q/2\nu = 3600$ or $Re_b = 7860$, where q denotes the flow rate per unit spanwise width in the channel. For reference, DNS studies were also performed in base turbulent channel flows with smooth, no-slip walls at the same Re_b as the SH channels. The corresponding friction Reynolds numbers in the base turbulent channel flows were $Re_{\tau_0} \equiv u_{\tau_0}h/\nu \approx 222$ at $Re_b = 3600$, and $Re_{\tau_0} \approx 442$ at $Re_b = 7860$.

A total of 53 simulations were performed with SH longitudinal microgrooves, covering the range of microgroove widths $4 \lesssim g^{+0} \lesssim 128$, solid fractions of $1/64 \leqslant \phi_s \leqslant 1/2$, protrusion angles of $\theta_p = 0°$ and $\theta_p = -30°$ and bulk Reynolds numbers of $Re_b = 3600$ ($Re_{\tau_0} \approx 222$) and $Re_b = 7860$ ($Re_{\tau_0} \approx 442$), as shown in table 1. In addition, as shown in table 1, four simulations were also performed with SH aligned square microposts with $g^{+0} \approx 28, 56$, $\phi_s = 1/64$ and $\theta_p = 0°$ at $Re_b = 3600$ ($Re_{\tau_0} \approx 222$) and $Re_b = 7860$ ($Re_{\tau_0} \approx 442$).

3. The scaling of drag reduction with surface microtexture and flow parameters

It has been suggested that in drag reduction with microtextured surfaces, be they riblets, SH surfaces or liquid-infused (LI) surfaces, the magnitude of drag reduction depends not only on the geometry and size of the surface microtexture in wall units, but also the Reynolds number of the base flow (Bechert *et al.* 1997; Spalart & McLean 2011; García-Mayoral & Jiménez 2012; Rastegari & Akhavan 2018*a*). It has also been suggested (Bechert *et al.* 1997; Spalart & McLean 2011) that a Reynolds number independent measure of drag reduction can be constructed by representing the normalized mean velocity profiles in the base flow and in the flow with microtextured walls as logarithmic profiles, $\langle \overline{U} \rangle / u_{\tau_0} = (1/\kappa) \ln z^{+0} + B_0$ and $\langle \overline{U} \rangle / u_\tau = (1/\kappa) \ln z^+ + B$, throughout the cross-section of the flow, and expressing the magnitude of drag reduction in terms of the shift, $(B - B_0)$, in the intercepts of these logarithmic-law representations of the mean velocity profiles, as shown in the figure 2. Here, and throughout this study, an overbar denotes Reynolds averaging in time and any homogeneous flow directions, and brackets $\langle \rangle$ denote averaging in the wall-parallel directions.

ϕ_s	g^{+0}	$DR\ (\theta_p = 0°)\ (\%)$	$DR\ (\theta_p = -30°)\ (\%)$
		SH longitudinal microgrooves, $Re_b = 3600$ ($Re_{\tau_0} \approx 222$)	
$1/2$	$4, 8, 16, 32, 64, 128$	$4.9, 10.4, 18.0, 19.2, 31.9, 42.4$	$-, 11.2, 18.5, 21.7, 33.9, 44.0$
$1/8$	$14, 28, 56$	$36.6, 48.1, 59.5$	$37.4, 51.7, 61.1$
$1/16$	$15, 30, 60, 120$	$46.0, 58.8, 69.9, 79.8$	$46.3, 60.3, 71.1, 80.1$
$1/32$	$62, 124$	$76.8, 85.4$	$76.7, 84.7$
$1/64$	$63, 126$	$81.5, 88.5$	$80.5, 87.5$
		SH longitudinal microgrooves, $Re_b = 7860$ ($Re_{\tau_0} \approx 442$)	
$1/8$	$14, 28$	$34.9, 46.3$	$36.6, 49.5$
$1/16$	$15, 30, 60, 120$	$44.4, 58.1, 67.7, 78.6$	$45.2, 59.3, 68.9, 78.5$
$1/32$	$62, 124$	$74.7, 83.8$	$75.2, 83.4$
$1/64$	$63, 126$	$79.8, 87.6$	$79.7, 86.6$
		SH aligned microposts, $Re_b = 3600$ ($Re_{\tau_0} \approx 222$)	
$1/64$	$28, 56$	$73.9, 80.7$	—
		SH aligned microposts, $Re_b = 7860$ ($Re_{\tau_0} \approx 442$)	
$1/64$	$28, 56$	$72.3, 79.2$	—

TABLE 1. Summary of simulation parameters and resulting drag reductions, *DR*, in the present study.

Using this formulation, the magnitude of drag reduction with microtextured surfaces can be expressed as (Rastegari & Akhavan 2018*a*)

$$(1 - DR) = \left\{ 1 + \left[\frac{1}{2\kappa} \ln(1 - DR) + (B - B_0) \right] \sqrt{\frac{C_{f_0}}{2}} \right\}^{-2}, \qquad (3.1)$$

where $DR \equiv 1 - C_f/C_{f_0}$ is the magnitude of drag reduction, C_f and C_{f_0} are the skin-friction coefficients in the flow with microtextured walls and in the base flow with smooth no-slip walls, defined as $C_f \equiv 2u_\tau^2/U_b^2$ and $C_{f_0} \equiv 2u_{\tau_0}^2/U_{b_0}^2$ in internal flow and $C_f \equiv 2u_\tau^2/U_\infty^2$ and $C_{f_0} \equiv 2u_{\tau_0}^2/U_\infty^2$ in external flow, respectively, κ is the von Kármán constant, and $(B - B_0)$ is Reynolds number independent and only a function of the geometry and size of the surface microtexture in wall units. The appearance of C_{f_0} in (3.1) leads to a degradation in the magnitude of drag reduction with increasing Reynolds number of the base flow for a given $(B - B_0)$.

It was brought to our attention by one of the anonymous referees that (3.1) can be recast into an explicit expression for *DR*, given by

$$DR = 1 - \kappa^2 \left(\frac{2}{C_{f_0}} \right) \left\{ W \left(\kappa \sqrt{\frac{2}{C_{f_0}}} \exp \left(\kappa \left[(B - B_0) + \sqrt{\frac{2}{C_{f_0}}} \right] \right) \right) \right\}^{-2}, \qquad (3.2)$$

where *W* denotes the Lambert *W* function.

Figure 3 shows the predictions of (3.1) in turbulent channel flow for $222 \lesssim Re_{\tau_0} \lesssim 10^6$ compared to results from present DNS studies in turbulent channel flows with SH longitudinal microgrooves or SH aligned microposts at $Re_{\tau_0} \approx 222$ and 442, as summarized in table 1. For $Re_{\tau_0} \geqslant 1000$, the values of C_{f_0} in (3.1) were obtained from the logarithmic skin-friction correlation suggested by Zanoun, Nagib & Durst
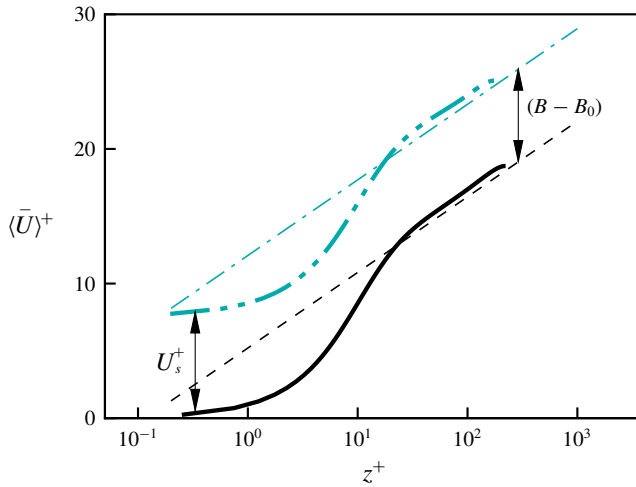
FIGURE 2. Schematic representation of $(B - B_0)$ and U_s^+ in turbulent flow with microtextured walls: —— (black), $-\cdot\cdot-$ (turquoise), mean velocity profiles in the base turbulent flow and the flow with microtextured walls, respectively; $---$ (black), $-\cdot-$ (turquoise), logarithmic representations of the mean velocity profiles in the base turbulent flow and the flow with microtextured walls, respectively.

(2009), which has been shown to give improved agreement with experimental data at high Reynolds numbers compared to the classical Dean's correlation (Dean 1978). In agreement with the predictions of (3.1), for a given value of $(B - B_0)$, the DNS data show small degradations of ≈ 1.0–2.5% in drag reduction as the friction Reynolds number of the base flow increases from $Re_{\tau_0} \approx 222$ to 442. Also shown in figure 3 are the experimental data of Zhang *et al.* (2015), obtained in turbulent boundary layer flow with SH random microposts at $Re_{\tau_0} \approx 460$ and 560, the experimental data of Ling *et al.* (2016), obtained in turbulent boundary layer flow with SH longitudinal microgrooves at $Re_{\tau_0} \approx 863$ or with SH random microposts at $Re_{\tau_0} \approx 863$, 1408 and 4287, and the experimental data of Srinivasan *et al.* (2015), obtained in turbulent Taylor–Couette flow with SH random microposts at $Re_{\tau_0} \approx 1193$ and 3810. In plotting these experimental data, the values of $(B - B_0)$ were approximated by the values of ΔU^+ reported in the experiments. Good agreement can be seen between the predictions of (3.1) and the experimental data, including the case where the SH surface gives a negative drag reduction of -10% in turbulent boundary layer flow at $Re_{\tau_0} \approx 4287$ (Ling *et al.* 2016). Evidence of the degradation of drag reduction with increasing Reynolds number of the base flow, for a given value of $(B - B_0)$, can also be seen in these experimental data. For example, in turbulent boundary layer flow with SH random microposts, a $(B - B_0) = 1.1$ is reported to give rise to 12% drag reduction at $Re_{\tau_0} \approx 863$, but only 11% drag reduction at $Re_{\tau_0} \approx 1408$ (Ling *et al.* 2016). Similarly, a $(B - B_0) = 3.2$ is found to give rise to 24.7% drag reduction in turbulent boundary layer flow with SH random microposts at $Re_{\tau_0} \approx 560$ (Zhang *et al.* 2015), but only 22% drag reduction in turbulent Taylor–Couette flow with SH random microposts at $Re_{\tau_0} \approx 3810$ (Srinivasan *et al.* 2015). While these degradations in drag reduction are small at moderate Reynolds number, they become far more significant at higher Reynolds numbers, requiring ever higher values of $(B - B_0)$ to achieve a given level of drag reduction, as shown in figure 3. Nevertheless, with a judicious choice
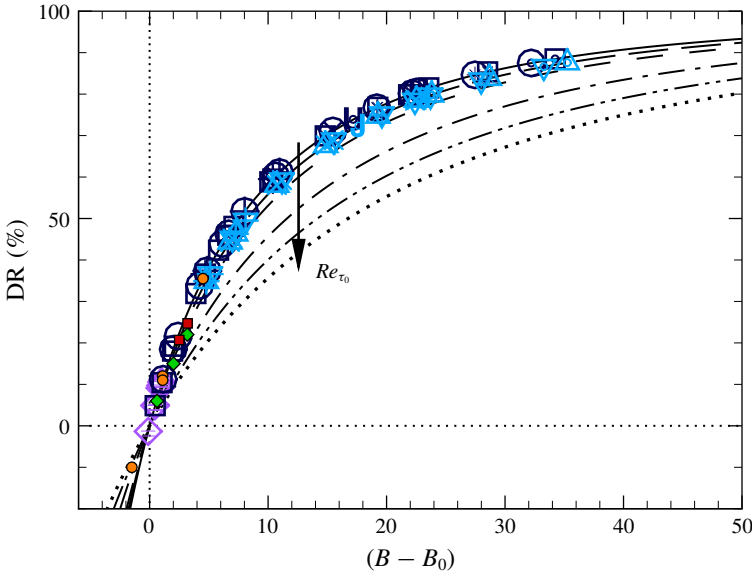
FIGURE 3. The magnitude of drag reduction, *DR*, as a function of $(B - B_0)$ and the friction Reynolds number of the base flow, Re_{τ_0}. Present DNS studies in SH turbulent channel flow: $\square$, $\boxplus$, $\boxtimes$, $\boxslash$, $\boxdot$ (navy), SH longitudinal microgrooves, $Re_{\tau_0} \approx 222$, $\theta_p = 0°$, $\phi_s = 1/2$, 1/8, 1/16, 1/32, 1/64; $\bigcirc$, $\oplus$, $\otimes$, $\circledast$, $\odot$ (navy), SH longitudinal microgrooves, $Re_{\tau_0} \approx 222$, $\theta_p = -30°$, $\phi_s = 1/2$, 1/8, 1/16, 1/32, 1/64; $\triangle\!\!\!\!+$, $\triangle\!\!\!\!\times$, $\triangle\!\!\!\!\equiv$, $\triangle$ (blue), SH longitudinal microgrooves, $Re_{\tau_0} \approx 442$, $\theta_p = 0°$, $\phi_s = 1/8$, 1/16, 1/32, 1/64; $\nabla\!\!\!\!+$, $\nabla\!\!\!\!\times$, $\nabla\!\!\!\!\equiv$, $\triangledown$ (blue), SH longitudinal microgrooves, $Re_{\tau_0} \approx 442$, $\theta_p = -30°$, $\phi_s = 1/8$, 1/16, 1/32, 1/64; $\cup\!\!\!|$ (navy), SH aligned microposts, $Re_{\tau_0} \approx 222$, $\theta_p = 0°$, $\phi_s = 1/64$; $\cup\!\!\!|$ (blue), SH aligned microposts, $Re_{\tau_0} \approx 442$, $\theta_p = 0°$, $\phi_s = 1/64$; $\diamondsuit\!\!\!\!\!\leftrightarrow$ (lavender), DNS of turbulent channel flow with LI longitudinal microgrooves, $Re_{\tau_0} \approx 180$, $\theta_p = 0^o$, $\phi_s = 1/2$, $N = 0.1$, 1, 2.5, 10, 20, 100 (Fu *et al.* 2017); $\blacksquare$ (red), experiments in turbulent boundary layer flow with SH random microposts, $Re_{\tau_0} \approx 460$ and 560 (Zhang *et al.* 2015); $\blacklozenge$ (green), experiments in turbulent Taylor–Couette flow with SH random microposts, $Re_{\tau_0} \approx 1193$ and 3810 (Srinivasan *et al.* 2015); $\bullet$ (orange), experiments in turbulent boundary layer flow with SH longitudinal microgrooves or SH random microposts, $Re_{\tau_0} \approx 863$, 1408 and 4287 (Ling *et al.* 2016). The black lines show the predictions of (3.1) in turbulent channel flow for: ——, $Re_{\tau_0} \approx 222$ ($Re_b = 3600$); — —, $Re_{\tau_0} \approx 442$ ($Re_b = 7860$); – – –, $Re_{\tau_0} = 10^3$ ($Re_b \approx 2 \times 10^4$); – ·–, $Re_{\tau_0} = 10^4$ ($Re_b \approx 2.6 \times 10^5$); – ··–, $Re_{\tau_0} = 10^5$ ($Re_b \approx 3.2 \times 10^6$); ······, $Re_{\tau_0} = 10^6$ ($Re_b \approx 3.8 \times 10^7$).

of $(B - B_0)$, drag reductions of up to $\sim 50\%$ should still be feasible at $Re_{\tau_0} \sim 10^5$–10^6 of practical interest. Finally, it should be noted that the drag reduction relation given by (3.1) is equally valid for all microtexture surfaces, including LI surfaces. This can be seen in figure 3 by a comparison of the predictions of (3.1) with the DNS results of Fu *et al.* (2017), obtained in turbulent channel flows with LI longitudinal microgrooves at viscosity ratios of $0.1 \leqslant N \equiv \mu_o/\mu_i \leqslant 100$ with $\phi_s = 1/2$, $\theta_p = 0°$ and $Re_{\tau_0} \approx 180$.

Designing optimal SH surfaces for drag reduction in high Reynolds number turbulent flows requires, in addition to (3.1), an understanding of the scaling of $(B - B_0)$ with the geometrical parameters of the surface microtexture. Progress can be
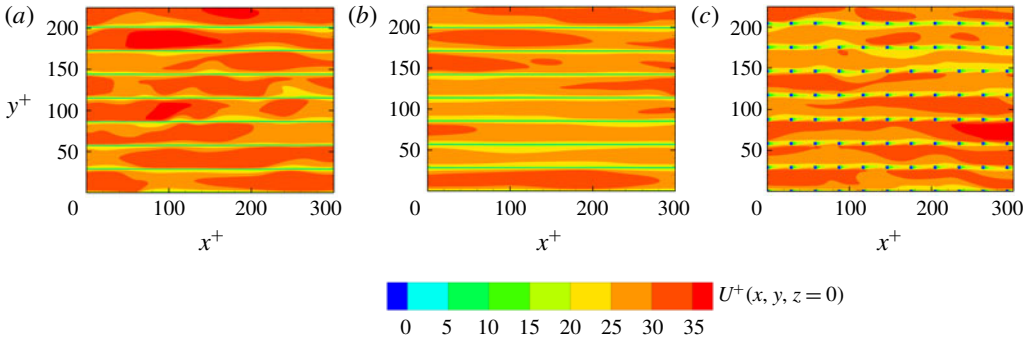
FIGURE 4. Contours of instantaneous streamwise velocity, $U^+(x, y, z)$, at $z = 0$ for: (*a*) SH longitudinal microgrooves, $Re_{\tau_0} \approx 442$, $\theta_p = 0°$, $\phi_s = 1/64$, $g^{+0} \approx 63$; (*b*) SH longitudinal microgrooves, $Re_{\tau_0} \approx 442$, $\theta_p = -30°$, $\phi_s = 1/64$, $g^{+0} \approx 63$; (*c*) SH aligned microposts, $Re_{\tau_0} \approx 442$, $\theta_p = 0°$, $\phi_s = 1/64$, $g^{+0} \approx 56$.

made by noting that the shift, $(B - B_0)$, arises primarily because of the presence of an effective streamwise slip velocity, U_s^+, at the wall, as shown in figure 2 (Min & Kim 2004; Seo & Mani 2016; Rastegari & Akhavan 2018*a*). However, the magnitude of $(B - B_0)$ is always smaller than U_s^+ due to concurrent presence of spanwise slip. As such, $(B - B_0)$ and U_s^+ can be expected to have similar scalings with surface microtexture geometrical parameters, but with a smaller multiplicative coefficient in the scaling law for $(B - B_0)$ compared to U_s^+.

The scaling of U_s^+ with surface microtexture parameters can be clarified by considering the dynamics of turbulence kinetic energy (TKE) within the 'surface layer'. This is a layer of thickness $\sim g$ above the microtextured walls, in which the flow transitions from the slip/no-slip patterns at the tip of the wall microtexture, at $z = 0$, to a homogeneous turbulent flow in the wall-parallel directions at $z \sim g$ (Rastegari & Akhavan 2015). For surface microtextures where the flow can find an unobstructed passageway through the surface micro-features, such as with longitudinal microgrooves or aligned microposts, sharp spanwise gradients of the mean streamwise velocity develop between the slip and no-slip regions of the boundary, giving rise to strong shear layers within the surface layer above these regions, as shown in figures 4(*a*–*c*), 5(*c*,*f*) and 6(*c*,*f*). These shear layers are the strongest with longitudinal microgrooves, but are also present with aligned microposts, where entire stripes aligned with the row of microposts can act as low-slip regions, as shown in figures 4(*c*) and 6(*c*,*f*). The presence of interface curvature somewhat mitigates the strength of these shear layers, but their mechanism is still at work, as can be seen by a comparison of figures 4(*a*) and 4(*b*) or figures 5(*c*) and 5(*f*).

These shear layers are the source of additional production of TKE within the surface layer through the $-\overline{uv} \, \partial \bar{U}/\partial y$ term, as shown in figures 5(*a*,*b*) and 6(*a*). This additional production of TKE, which is above and beyond the normal production of TKE in wall-bounded flows through the $-\overline{uw} \, \partial \bar{U}/\partial z$ term, dominates the overall production of TKE within the surface layer, as shown in figures 5(*a*,*b*,*d*,*g*) and 6(*a*,*d*,*g*). The additional production of TKE through these shear layers is dissipated by the turbulent eddies above the no-slip regions, as shown in figures 5(*e*,*h*) and 6(*e*,*h*), such that

$$\{-\overline{uv} \, \partial \bar{U}/\partial y\}_{shear\,layers} \sim \{\nu \overline{s_{ij} s_{ij}}\}_{no\text{-}slip}. \tag{3.3}$$
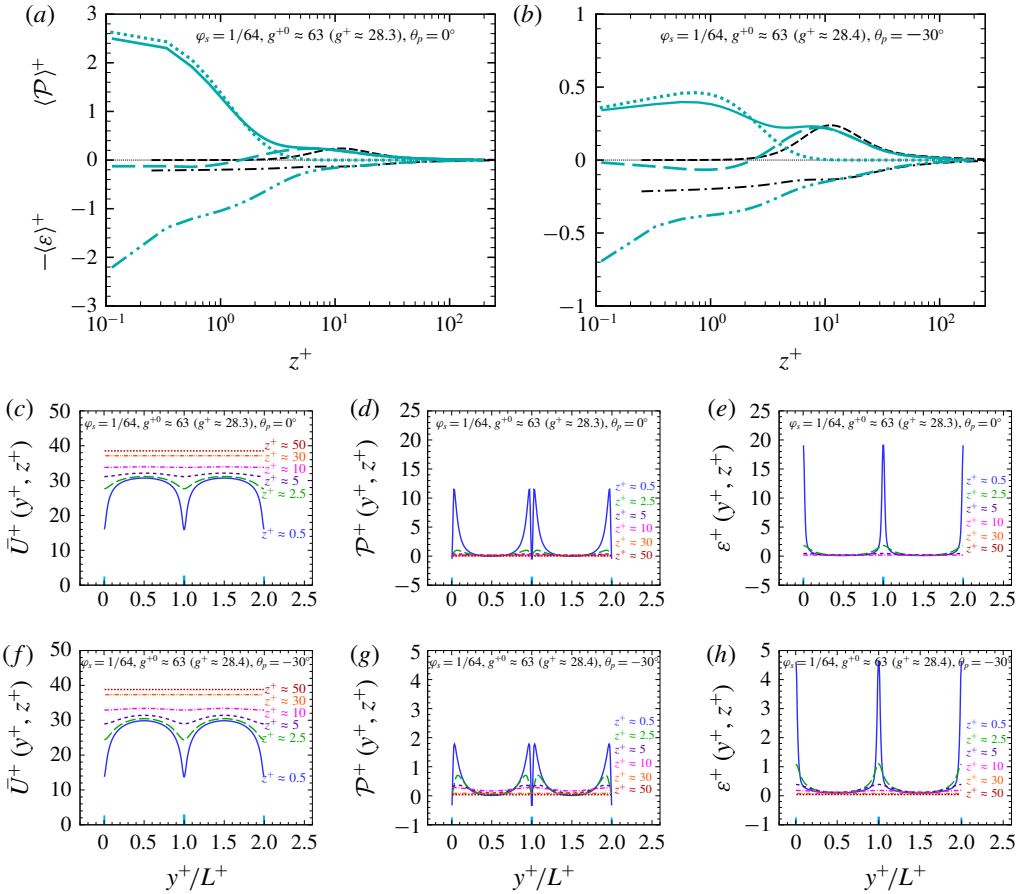
FIGURE 5. Production and dissipation of turbulence kinetic energy in turbulence channel flow with SH longitudinal microgrooves at (a,c,d,e) $Re_{\tau_0} \approx 442$, $\theta_p = 0°$, $\phi_s = 1/64$, $g^{+0} \approx 63$ and (b,f,g,h) $Re_{\tau_0} \approx 442$, $\theta_p = -30°$, $\phi_s = 1/64$, $g^{+0} \approx 63$: (a,b) ——, ——, ·······, –··– (turquoise), total production $\langle \mathcal{P} \rangle^+ = -\langle \overline{u_i u_j} \bar{S}_{ij} \rangle^+$, production arising from $-\langle \overline{uw} \partial \bar{U}/\partial z \rangle^+$, production arising from $-\langle \overline{uv} \partial \bar{U}/\partial y \rangle^+$, dissipation $\langle \varepsilon \rangle^+ = \langle 2\nu \overline{s_{ij} s_{ij}} \rangle^+$, in turbulent channel flow with SH walls; –––, –·– (black), production arising from $-\langle \overline{uw} \partial \bar{U}/\partial z \rangle^+$ and dissipation, $\langle \varepsilon \rangle^+$, in base turbulent channel flow with smooth, no-slip walls; $(c,d,e; f,g,h)$ spanwise variation of the mean streamwise velocity, $\bar{U}^+$, total production, $\mathcal{P}^+$, and dissipation, ε^+, at different z^+ in turbulent channel flow with SH longitudinal microgrooves at $\theta_p = 0°$ and $\theta_p = -30°$, respectively. The blue bars on the lower horizontal axes of $(c–h)$ denote the locations of the no-slip surfaces. $L = g + w$ denotes the pitch of the microgrooves.

An order of magnitude estimate of the terms in (3.3) leads to the scaling law for U_s^+. Specifically, within the surface layer, the spanwise gradients of the mean streamwise velocity can be estimated as $\partial \bar{U}/\partial y \sim U_{ss}/g$, where $U_{ss} = U_s/(1 - \phi_s)$ is the average slip velocity on the slip portions of the microtextured walls. Furthermore, the fluctuating strain rate above the no-slip regions can be estimated as $\{s_{ij}\}_{no-slip} \sim \sqrt{u_{\tau_n} u_\tau}/(\nu/\sqrt{u_{\tau_n} u_\tau})$, where $\sqrt{u_{\tau_n} u_\tau}$ is the characteristic velocity of the turbulent eddies
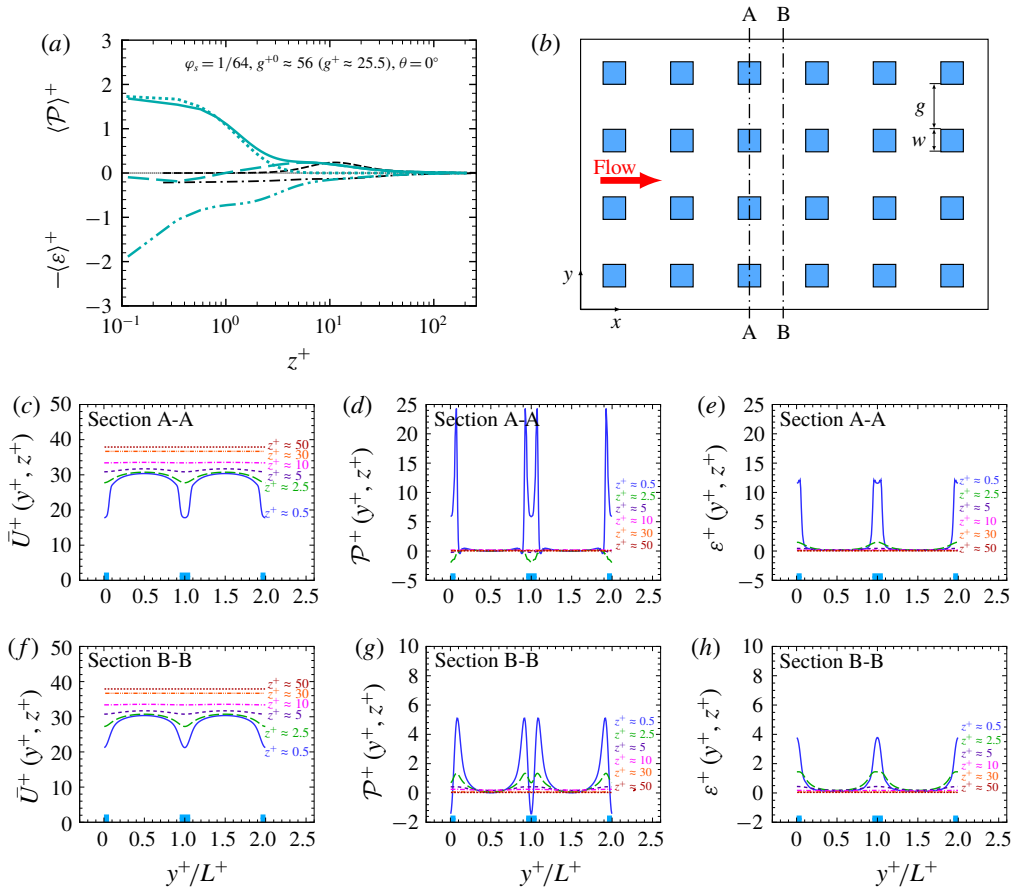
FIGURE 6. Production and dissipation of turbulence kinetic energy in turbulent channel flow with SH aligned microposts at $Re_{\tau_0} \approx 442$, $\theta_p = 0°$, $\phi_s = 1/64$, $g^{+0} \approx 56$: (a) total production $\langle \mathcal{P} \rangle^+ = -\langle \overline{u_i u_j} \overline{S}_{ij} \rangle^+$, production arising from $-\langle \overline{uw} \partial \bar{U}/\partial z \rangle^+$, production arising from $-\langle \overline{uv} \partial \bar{U}/\partial y \rangle^+$, dissipation $\langle \varepsilon \rangle^+ = \langle 2\nu \overline{s_{ij} s_{ij}} \rangle^+$, in turbulent channel flow with SH walls, compared to base turbulent channel flow with smooth, no-slip walls; (b) schematic representation of sections A-A and B-B where turbulence statistics are shown in (c–e) and (f–h); (c–e; f–h) spanwise variation of the mean streamwise velocity, $\bar{U}^+$, total production, $\mathcal{P}^+$, dissipation, ε^+, at different z^+ of sections A-A and B-B, respectively. Line types in (a) as in figure 5. The blue bars on the lower horizontal axes of (c–h) denote the locations of the no-slip surfaces. $L = g + w$ denotes the pitch of the microposts.

above the no-slip regions within the surface layer, estimated as the geometric average of the wall friction velocities $u_{\tau_n} = u_\tau / \sqrt{\phi_s}$ and u_τ above the no-slip regions at $z = 0$ and $z \sim g$, respectively, and $\nu / \sqrt{u_{\tau_n} u_\tau}$ is the associated inner length scale. Finally, the Reynolds shear stress $-\overline{uv}$ can be estimated using a mixing-length model as $-\overline{uv} \sim \nu_t \partial \bar{U}/\partial y \sim u' \ell \ \partial \bar{U}/\partial y$, where $u' \sim \sqrt{u_{\tau_n} u_\tau}$ is the characteristic velocity of the largest eddies within the surface layer, and $\ell \sim \sqrt{g\nu/u_\tau}$ is their characteristic size, approximated as the geometric average of g and ν/u_τ, representing the size of the largest eddies at $z \sim g$ and $z \sim 0$, respectively. Substitution of these expressions into

(3.3) gives the scaling law for U_s^+ as

$$\frac{\phi_s^{3/8}}{(1 - \phi_s)} U_s^+ \sim \{g^+\}^{3/4}. \tag{3.4}$$

Given that the dominant contribution to $(B - B_0)$ arises from U_s^+, a similar scaling can also be assumed for $(B - B_0)$:

$$\frac{\phi_s^{3/8}}{(1 - \phi_s)} (B - B_0) \sim \{g^+\}^{3/4}, \tag{3.5}$$

with the understanding that the multiplicative coefficient in the expression for $(B - B_0)$ would be smaller than that for U_s^+.

Figure 7(a–d) shows U_s^+ and $(B - B_0)$ from the DNS studies summarized in table 1, compared to (3.4) and (3.5). At both $Re_{\tau_0} \approx 222$ and 442, and for both $\theta_p = 0°$ and $\theta_p = -30°$, U_s^+ and $(B - B_0)$ scale as $\{g^+\}^{3/4}$, while normalization with $\phi_s^{3/8}/(1 - \phi_s)$ collapses the data from different ϕ_s. Both U_s^+ and $(B - B_0)$ are Reynolds number independent and only functions of the geometrical parameters of the surface microtexture in wall units, in agreement with the predictions of (3.4) and (3.5).

A best fit to the DNS data gives the multiplicative coefficients in the expressions for U_s^+ and $(B - B_0)$ as

$$U_s^+ = 0.52\{(1 - \phi_s)\phi_s^{-3/8}\}\{g^+\}^{3/4}, \tag{3.6}$$

$$(B - B_0) = 0.41\{(1 - \phi_s)\phi_s^{-3/8}\}\{g^+\}^{3/4}, \tag{3.7}$$

with *p*-values of 0.98, obtained from the Kolmogorov–Smirnov goodness of fit test.

Figure 7(e,f) shows the comparison of (3.6) and (3.7) with available DNS data from other investigators, obtained in turbulent channel flows using SH longitudinal microgrooves (Park *et al.* 2013), SH aligned microposts (Seo & Mani 2016) or LI longitudinal microgrooves at viscosity ratios of $N \equiv \mu_o/\mu_i = 0.1, 1, 10, 20, 100$ (Fu *et al.* 2017). Good agreement can be seen between the predictions of (3.6) and (3.7) and available DNS data from other investigators for both SH longitudinal microgrooves and SH aligned microposts as long as $g^+ < 100$. For $g^+ > 100$, both U_s^+ and $(B - B_0)$ saturate and branch off from the predictions of (3.6) and (3.7). This saturation has been attributed to the width of the microgrooves, g^+, approaching the mean streak spacing of $\lambda^+ \sim 100$ in turbulent wall flows (Park *et al.* 2013). Presumably, for $g^+ \gtrsim 100$, the dynamics of turbulence above the slip regions becomes independent of the dynamics of turbulence above the no-slip regions, and both U_s^+ and $(B - B_0)$ approach their limiting values.

Good agreement can also be seen in figure 7(e,f) between the predictions of (3.6) and (3.7) and DNS results in turbulent channel flows with LI longitudinal microgrooves (Fu *et al.* 2017) when the viscosity ratio, N, is greater than ~ 10. These results suggest that for high enough viscosity ratios, of $N \gtrsim 10$, the drag reduction of LI surfaces begins to approach that of SH surfaces. These findings are consistent with analytical solutions in laminar shear flow with LI surfaces obtained by Schönecker, Baier & Hardt (2014), and reproduced in figure 8, which show that for LI longitudinal microgrooves of depth $d = g$, $\phi_s = 0.5$ and viscosity ratio of $N = 10$, the effective slip length is $\approx 86\%$ of the effective slip length predicted by Philip's solution (Philip 1972) for the same surface microtexture with 'idealized', shear-free, SH interfaces. The LI results shown in figure 7(e,f) are also consistent
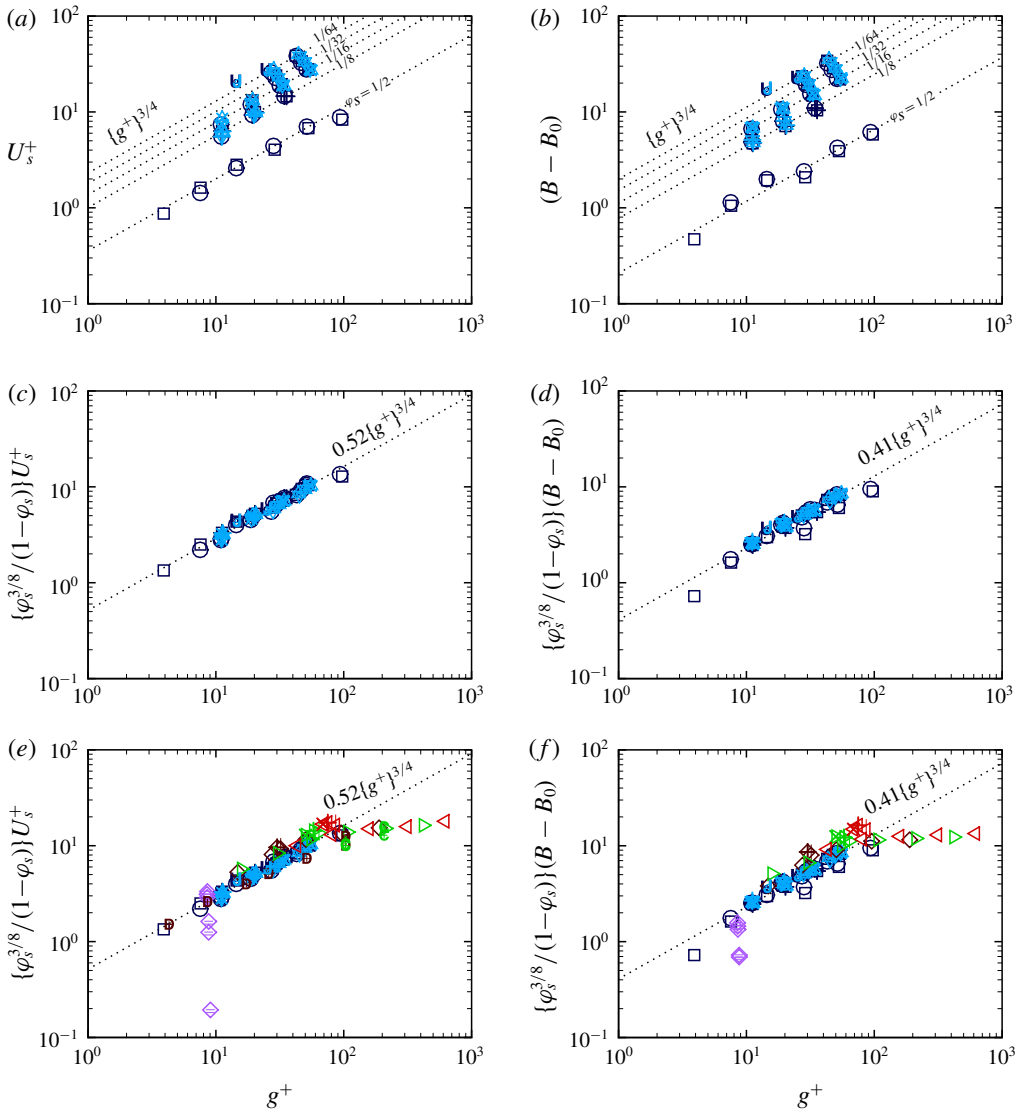
FIGURE 7. The scaling of U_s^+ and $(B - B_0)$ with surface microtexture parameters in turbulent flow with SH or LI walls: (a–d) present DNS data in turbulent channel flow with SH longitudinal microgrooves or SH aligned microposts at $Re_{\tau_0} \approx 222$ and 442, $1/64 \leqslant \phi_s \leqslant 1/2$, $\theta_p = 0°$ and $-30°$; (e,f) DNS data from other investigators in turbulent channel flow with SH longitudinal microgrooves, LI longitudinal microgrooves or SH aligned microposts at $180 \lesssim Re_{\tau_0} \lesssim 590$, $1/36 \leqslant \phi_s \leqslant 1/2$. Symbols as in figure 3. Other symbols in (e,f): $\oplus$, $\oplus$, $\diamondsuit$ (brown), $Re_{\tau_0} \approx 180$, $\phi_s = 1/8$, 1/4, 1/2, $\bowtie$, $\oplus$, $\triangleright$, $\triangleright$ (green), $Re_{\tau_0} \approx 395$, $\phi_s = 1/16$, 1/8, 1/4, 1/2, $\triangleleft$, $\oplus$, $\triangleleft$, $\triangleleft$ (red), $Re_{\tau_0} \approx 590$, $\phi_s = 1/16$, 1/8, 1/4, 1/2, SH longitudinal microgrooves, $\theta_p = 0°$ (Park *et al.* 2013); $\ominus$, $\oplus$ (brown), $Re_\tau \approx 195$, $\phi_s = 1/64$, 1/9, $\oplus$, $\oplus$, $\oplus$ (green), $Re_\tau \approx 400$, $\phi_s = 1/36$, 1/16, 1/9, SH aligned microposts, $\theta_p = 0°$ (Seo & Mani 2016).
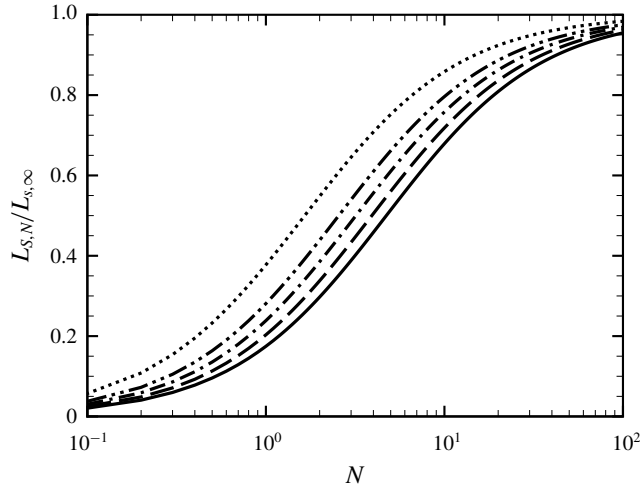
FIGURE 8. Ratio of the effective slip length, $L_{s,N}$, obtained with a finite viscosity ratio, N, based on the analytical solution of Schönecker *et al.* (2014), to the effective slip length, $L_{s,\infty}$, obtained with the assumption of shear-free liquid/air interfaces (Philip 1972), in laminar shear flow over LI longitudinal microgrooves for groove depth $d = g$ and $1/64 \leqslant \phi_s \leqslant 1/2$: $\cdots\cdots$, $\phi_s = 1/2$; — $\cdot\cdot$ —, $\phi_s = 1/8$; — $\cdot$ —, $\phi_s = 1/16$; – – –, $\phi_s = 1/32$; ——, $\phi_s = 1/64$.

with experimental measurements in turbulent Taylor–Couette flow with LI longitudinal microgrooves of depth $d = g$, $\phi_s = 0.5$ and $0.7 \leqslant N \leqslant 3.0$ (Van Buren & Smits 2017), which show the drag reduction of the LI surface at $N \approx 2.0$–3.0 to be ≈ 50–60% of the drag reduction of a SH surface with the same surface microtexture.

In the derivation of (3.6) and (3.7), the multiplicative coefficients, of 0.52 and 0.41, were obtained based on DNS data which assumed 'idealized', shear-free boundaries at the air/water interfaces and, as such, did not consider the flow of air in the SH microgrooves. This raises a concern that the magnitudes of U_s^+ and $(B - B_0)$ would be over-predicted by (3.6) and (3.7). An estimate of the degree of this over-prediction can be obtained by comparing analytical solutions for the effective slip length, $L_{s,N}$, obtained with a finite viscosity ratio, N, in laminar shear flow with LI longitudinal microgrooves (Schönecker *et al.* 2014) to the effective slip length, $L_{s,\infty}$, which would be predicted in the same flow based on the assumption of shear-free liquid/air interfaces (Philip 1972). Figure 8 shows $L_{s,N}/L_{s,\infty}$ as a function of N for longitudinal microgrooves of depth $d = g$ and the range of solid fractions, $1/64 \leqslant \phi_s \leqslant 1/2$, investigated in the present study. It can be seen that for $N \approx 56$, corresponding to air/water interfaces, the ratio $L_{s,N}/L_{s,\infty}$ ranges from $0.92 \leqslant L_{s,N}/L_{s,\infty} \leqslant 0.97$ for $1/64 \leqslant \phi_s \leqslant 1/2$. These results suggest that for the range of $1/64 \leqslant \phi_s \leqslant 1/2$, considered in the present study, the errors in (3.6) and (3.7) due to the assumption of shear-free interfaces are no more than 10 %. These errors can become larger for solid fractions of $\phi_s \lesssim 1/64$ or for shallow grooves of $d \lesssim g/2$ (Schönecker *et al.* 2014). However, such configurations of microgrooves are impractical to build, either because the microgroove blades become too thin to be structurally sustainable, or because the depth of the grooves becomes so shallow that the air/water interfaces can hit the bottom of the grooves during their deformation, thus expediting their collapse.

Another concern is the effect of dynamic deformation of the interface on (3.6) and (3.7), as the multiplicative coefficients in (3.6) and (3.7) were obtained from DNS
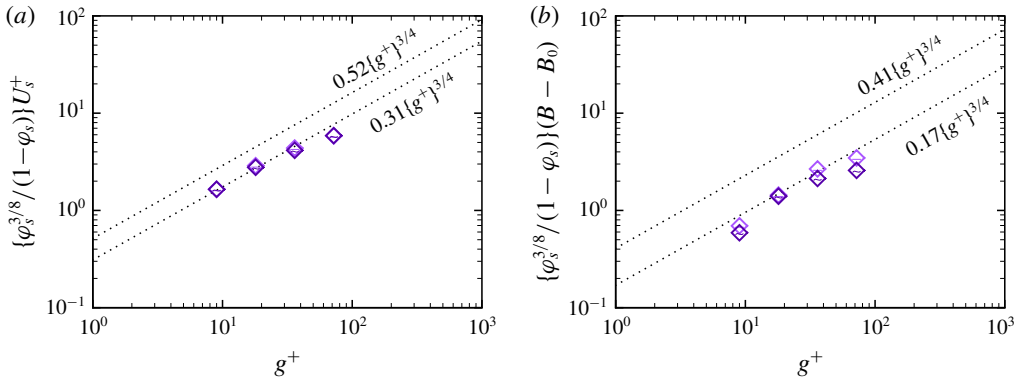
FIGURE 9. Effect of dynamic deformation of the interface on (*a*) U_s^+ and (*b*) $(B - B_0)$, based on DNS results with deformable interfaces, but pinned contact lines, in turbulent channel flows with LI longitudinal microgrooves at $Re_\tau \approx 180$, $\phi_s = 1/2$, $N = 2.5$ (Arenas-Navarro 2017): ◇ (lavender), $We_\tau = 0$; ◇ (dark violet), $We_\tau = 0.024$.

studies which were performed with 'stationary', flat or curved, shear-free interfaces. The effect of dynamic deformation of the interface can be assessed by examining available DNS results obtained with deformable interfaces, but pinned contact lines, in turbulent channel flows with LI longitudinal microgrooves at a viscosity ratio of $N = 2.5$ for $We_\tau = 0$ and $We_\tau = 0.024$ (Arenas-Navarro 2017), where $We_\tau \equiv \rho_o u_\tau v_o / \sigma$ is the Weber number, ρ_o and v_o are the density and kinematic viscosity of the outer fluid, respectively, and σ is the surface tension.

Figure 9 shows $\{\phi_s^{3/8}/(1 - \phi_s)\} U_s^+$ and $\{\phi_s^{3/8}/(1 - \phi_s)\} (B - B_0)$ computed from these DNS databases. Both $\{\phi_s^{3/8}/(1 - \phi_s)\} U_s^+$ and $\{\phi_s^{3/8}/(1 - \phi_s)\} (B - B_0)$ can be seen to scale as $\sim g^+\{^{3/4}\}$, in agreement with (3.6) and (3.7). However, the multiplicative coefficients in the best fit lines to the LI data are smaller than those in (3.6) and (3.7) by a factor of 0.6 for U_s^+ and a factor of 0.4 for $(B - B_0)$. These factors are comparable to the ratio $L_{s,N}/L_{s,\infty} = 0.6$ observed for $N = 2.5$ and $\phi_s = 1/2$ in figure 8.

The dynamic deformation of the interface is seen to have little effect on the slip velocity, with the values for U_s^+ at the two Weber numbers being nearly identical, as seen in figure 8(*a*). However, the surface ripples formed by the dynamic deformation of the interface can act as 'surface roughness' and reduce the magnitude of $(B - B_0)$ by $2.5 - 25.5\%$ at $We_\tau = 0.024$ compared to $We_\tau = 0$, as seen in figure 8(*b*). The results shown in figure 9 were obtained with LI longitudinal microgrooves at $N = 2.5$ and pinned contact lines. As will be shown in § 4 (figure 12), for SH longitudinal microgrooves, a $We_\tau = 0.024$ is very large and will lead to interface instability for $g^+ > 6.5$ at $Re_\tau \approx 200$. Stable SH longitudinal microgrooves require much smaller values of We_τ, for which the effect of dynamic deformation of the interface on $(B - B_0)$ is much smaller than the results shown in figure 8(*b*). Nevertheless, these effects can be accounted for by constructing a ΔB_k associated with the 'roughness' of the liquid/gas interface, and subtracting this ΔB_k from the $(B - B_0)$ given by (3.7) to get the drag reduction. More recent DNS studies (Rastegari & Akhavan 2018*b*) suggest that the motion of the contact line may be a more important source of roughness effects. A similar procedure can also be used to account for the roughness effects arising from the motion of the contact line on SH or LI longitudinal microgrooves or aligned microposts, assuming the interface has not fully collapsed.

Finally, it should be noted that, given that the derivations of (3.6) and (3.7) require an unobstructed passageway through the surface microtexture, these scalings are not expected to apply to staggered microposts or transverse microgrooves.

4. Sustainability bounds of superhydrophobic surfaces

Equations (3.1) and (3.7) provide a tool for *a priori* prediction of the magnitude of drag reduction with any pattern of SH longitudinal microgrooves or aligned microposts in turbulent flow at any Reynolds number. However, design of optimal SH surfaces also requires consideration of the sustainability bounds of such surfaces, as all SH surfaces are susceptible to a wetting transition from the Cassie–Baxter state to a Wenzel state. This wetting transition can occur because of (i) depinning of the contact line and/or sagging of the liquid–gas interface under high local pressures (Zheng *et al.* 2005; Checco *et al.* 2014) or (ii) diffusion or entrainment of the gas layer into the working liquid under high local shear rates (Samaha *et al.* 2012; Karatay *et al.* 2013; Wexler *et al.* 2015; Ling *et al.* 2017) of turbulent flow. Of the two mechanisms, the wetting transition due to high local pressures is generally the first mode of failure, and of the different SH surface microtextures, longitudinal microgrooves are the most stable under this mode of failure, as impingement of the flow on the back of microposts creates large stagnation pressures which can expedite the wetting transition (Seo, García-Mayoral & Mani 2015). Consequently, in this section we will focus only on the pressure stability bounds of SH longitudinal microgrooves.

For SH longitudinal microgrooves with stable interfaces, the contact line is pinned and the shape of the interface is governed by the Young–Laplace equation

$$\Delta P = -\frac{\sigma}{R} = -\frac{2\sigma \cos(\theta_c)}{g}, \qquad (4.1)$$

where ΔP is the pressure difference across the interface, σ is the surface tension, R is the radius of curvature of the interface, θ_c is the contact angle and g is the microgroove width. With increasing ΔP, the contact angle increases until it reaches the maximum advancing contact angle, $\theta_{F,adv}$, at which point the contact line depins (Checco *et al.* 2014). Assuming a maximum advancing contact angle of $\theta_{F,adv} = 120°$ (Nishino *et al.* 1999), the criterion for stability of SH interfaces becomes $\Delta Pg/\sigma \leqslant 1$, or

$$(\Delta P^+)(g^+)(We_\tau) \leqslant 1, \qquad (4.2)$$

where $\Delta P^+ \equiv \Delta P/(\rho u_\tau^2)$ is the non-dimensional pressure, and $We_\tau \equiv \rho u_\tau \nu/\sigma$ is the Weber number.

Assessing the stability bounds of SH surfaces in turbulent flow from (4.2) requires a knowledge of ΔP^+. In turbulent flow, ΔP^+ arises from the instantaneous pressure fluctuations on the SH walls. The range of values assumed by the instantaneous pressure fluctuations on the SH walls can be assessed by examining the probability density function (p.d.f.) of the wall pressure fluctuations, $f_p(p_w^+/\{\langle \overline{p^2}\rangle_w^+\}^{1/2})$. Figure 10(*a*) shows the p.d.f. of wall pressure fluctuations in turbulent channel flow with SH longitudinal microgrooves at $Re_{\tau_0} \approx 442$, $\phi_s = 1/64$, $g^{+0} \approx 63$ and $\theta_p = 0°$ and $\theta_p = -30°$, compared to turbulent channel flow with smooth, no-slip walls. The p.d.f. of instantaneous wall pressure fluctuations in turbulent channel flow with SH walls is found to be similar to that for smooth, no-slip walls. Both p.d.f.s follow a non-Gaussian distribution with exponential tails. Similar non-Gaussian
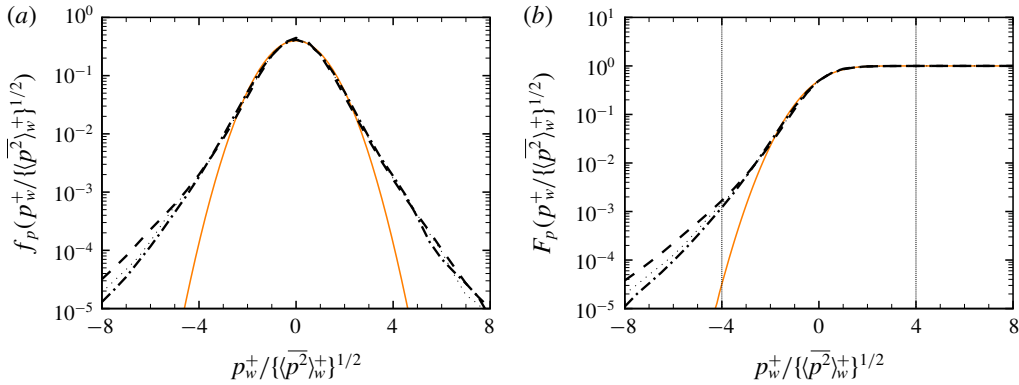
FIGURE 10. Probability density function and cumulative distribution function of the wall pressure fluctuations in turbulent channel flow with SH longitudinal microgrooves, compared to turbulent channel flow with smooth, no-slip walls: (*a*) probability density function, $f_p(p_w^+/\{\langle\overline{p^2}\rangle_w^+\}^{1/2})$; (*b*) cumulative distribution function, $F_p(p_w^+/\{\langle\overline{p^2}\rangle_w^+\}^{1/2})$; ---, -·-, SH longitudinal microgrooves, $Re_{\tau_0} \approx 442$, $\phi_s = 1/64$, $g^{+0} \approx 63$, $\theta_p = 0°$ and $-30°$, respectively; ·····, base turbulent channel flow with smooth, no-slip walls, $Re_{\tau_0} \approx 442$; —— (orange), Gaussian distribution.

distributions have also been reported experimentally in high Reynolds number turbulent boundary layers (Tsuji *et al.* 2007). The probability that the instantaneous pressure fluctuations fall within a given range of values, $a \leqslant p_w^+/\{\langle\overline{p^2}\rangle_w^+\}^{1/2} < b$, can be estimated from $F_p(b) - F_p(a) = \int_a^b f_p(\eta)\,\mathrm{d}\eta$, where F_p is the cumulative distribution function. Figure 10(*b*) shows the cumulative distribution functions, $F_p(p_w^+/\{\langle\overline{p^2}\rangle_w^+\}^{1/2})$, for the cases shown in figure 10(*a*). Examination of these cumulative distribution functions shows that the probability of the instantaneous wall pressure fluctuations falling within $\pm 4\{\langle\overline{p^2}\rangle_w^+\}^{1/2}$ is 99.75 %. These results are consistent with experimental measurements in turbulent boundary layer flows (Schewe 1983), which show a probability of 99.7 % for the wall pressure fluctuations never exceeding $4\{\overline{p_w^2}^+\}^{1/2}$. Based on these results, an upper estimate for the magnitude of ΔP^+ can be obtained as $\Delta P^+ \approx 4\{\langle\overline{p^2}\rangle_{w,SH}^+\}^{1/2}$, with 99.75 % confidence that the instantaneous wall pressure fluctuations will not exceed this value.

Figure 11(*a*) shows $\langle\overline{p^2}\rangle_{w,SH}^+$ as a function of Re_τ from present DNS studies of turbulent channel flow with SH longitudinal microgrooves at fixed protrusion angle of $\theta_p = -30°$ ($\theta_c = 120°$). For reference, the fit $\langle\overline{p^2}\rangle_{w,smooth}^+ = 2.31 \ln(Re_\tau) - 9.5$, suggested by Sillero *et al.* (2013), for turbulent channel flow with smooth no-slip walls is also shown. Similar to turbulent flow with smooth no-slip walls, the mean-squared wall pressure fluctuations in turbulent flow with SH walls is strongly Reynolds number dependent. However, due to the presence of spanwise slip, the magnitude of $\langle\overline{p^2}\rangle_{w,SH}^+$ on SH walls is higher than that on smooth no-slip walls at comparable Re_τ. Analysis of DNS data suggests that the effect of this spanwise slip can be captured in a function $\Gamma(g^+)$, such that

$$\langle\overline{p^2}\rangle_{w,SH}^+ \approx \Gamma(g^+) + \langle\overline{p^2}\rangle_{w,smooth}^+ \approx \Gamma(g^+) + 2.31 \ln(Re_\tau) - 9.5. \qquad (4.3)$$
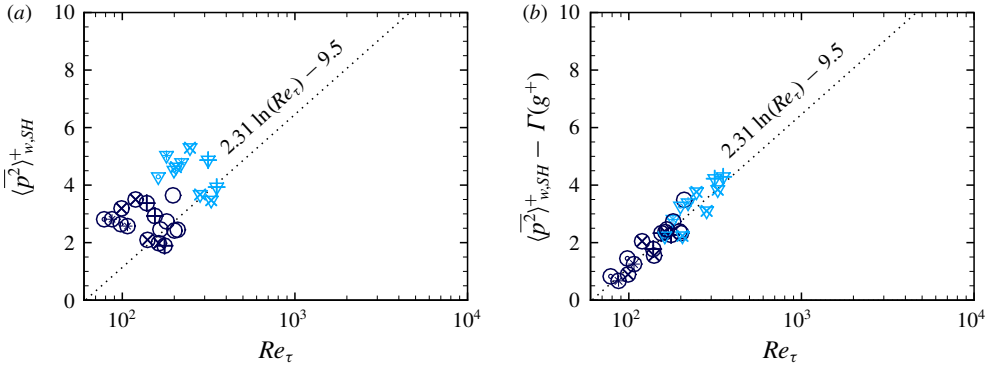
FIGURE 11. Mean-squared turbulent wall pressure fluctuations in turbulent channel flow with SH longitudinal microgrooves: (*a*) $\langle \overline{p^2} \rangle^+_{w,SH}$ as a function of Re_τ; (*b*) $\langle \overline{p^2} \rangle^+_{w,SH} - \Gamma(g^+)$ as a function of Re_τ, where $\Gamma(g^+) = 2.32\ln(\{g^+\}^{3/4}) - 4.5$. Symbols as in figure 3. ······, the fit $\langle \overline{p^2} \rangle^+_{w,smooth} = 2.31\ln(Re_\tau) - 9.5$, suggested by Sillero, Jiménez & Moser (2013) for turbulent channel flows with smooth, no-slip walls.

A best fit to the DNS data suggests the correlation

$$\Gamma(g^+) \approx \begin{cases} 2.32\ln(\{g^+\}^{3/4}) - 4.5, & g^+ \gtrsim 5 \\ 0, & g^+ \lesssim 5. \end{cases} \tag{4.4}$$

For $g^+ \lesssim 5$, the microgrooves become too narrow to generate any significant spanwise slip (Rastegari & Akhavan 2018*a*) and $\Gamma(g^+) \approx 0$. The correlations (4.3)–(4.4) fit the DNS data with a *p*-value of 0.97, based on the Kolmogorov–Smirnov goodness of fit test. Figure 11(*b*) shows the comparison of these correlations to the DNS data.

Figure 12 shows the pressure stability bounds of SH longitudinal microgrooves obtained from (4.2), with ΔP^+ approximated as $\Delta P^+ \approx 4\{\langle \overline{p^2} \rangle^+_{w,SH}\}^{1/2}$ and $\langle \overline{p^2} \rangle^+_{w,SH}$ computed from (4.3) to (4.4). Due to the strong Reynolds number dependence of $\langle \overline{p^2} \rangle^+_{w,SH}$, the pressure stability bounds of SH surfaces become significantly curtailed with increasing Reynolds number of the flow. Specifically, for the range of $10^4 \lesssim Re_{\tau_0} \lesssim 10^5$ and $We_{\tau_0} \approx 5 \times 10^{-3}$, typical of practical applications, figure 3 shows that achieving $\sim$50 % drag reduction requires a $(B - B_0) \approx 12$–14. At the same time, figure 12 shows that the microgroove widths should be kept to $g^+ \lesssim 17$–20 to maintain the stability of the interface. The only way such large values of $(B - B_0)$ can be achieved with such small values of g^+ is by using 'blade' or 'scalloped' longitudinal microgrooves with $\phi_s \lesssim 0.02$–0.05, per (3.7), where the nomenclature for 'blade' or 'scalloped' longitudinal microgrooves is borrowed from the riblet literature (Bechert *et al.* 1997).

The combination of (3.1), (3.7), (4.2) and (4.3)–(4.4) provides a set of design tools for *a priori* prediction of the magnitude of drag reduction and the sustainability bounds of SH surfaces in high Reynolds number turbulent flows. Given the Reynolds number, Re_{τ_0}, and Weber number, We_{τ_0}, of the base flow and a desired level of drag reduction, (3.1) provides an estimate of the required $(B - B_0)$, while (4.2) and (4.3)–(4.4) provide an estimate of the maximum groove width g^+ for stability. These $(B - B_0)$ and g^+ values can then be used in (3.7) to determine the maximum allowable solid fraction, ϕ_s.
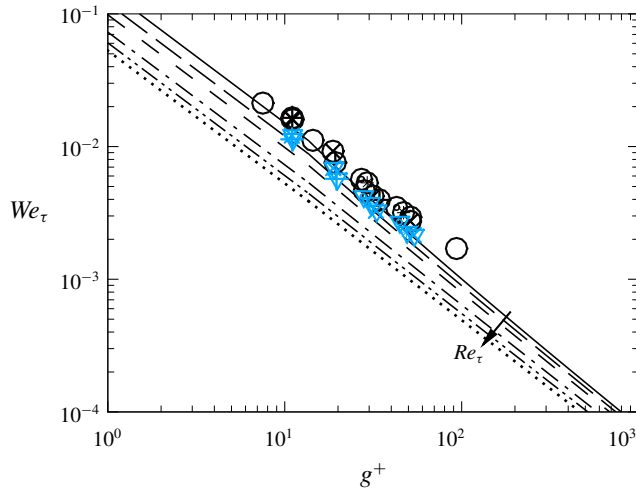
FIGURE 12. The maximum permissible We^+ and g^+ at a given Re_τ to maintain the stability of SH longitudinal microgrooves in turbulent channel flow. Lines show the predictions of (4.2) for: ——, $Re_\tau \approx 200$; — —, $Re_\tau \approx 400$; – – –, $Re_\tau \approx 10^3$; — · —, $Re_\tau \approx 10^4$; – · · –, $Re_\tau \approx 10^5$; · · · · · ·, $Re_\tau \approx 10^6$.

5. Summary and conclusions

Using scaling arguments and analysis of results from DNS, we present scaling laws which allow for *a priori* prediction of the magnitude of skin-friction drag reduction with SH or LI surfaces and the pressure stability bounds of SH surfaces in turbulent flow. It is shown that the magnitude of drag reduction can be parameterized in terms of the friction coefficient of the base flow and the shift, $(B - B_0)$, in the intercept of logarithmic-law representations of the mean velocity profiles in the flow with SH or LI walls compared to the base flow, where $(B - B_0)$ is Reynolds number independent. The parameterization of $(B - B_0)$ in terms of the geometrical parameters of the SH or LI surface, and the pressure stability bounds of SH longitudinal microgrooves in turbulent flow are presented. It is shown that, for a given geometry and size of the surface microtexture in wall units, both the magnitude of drag reduction and the sustainability bounds of SH surfaces degrade with increasing Reynolds number of the base flow. Using these scalings, the narrow range of surface microtexture geometrical parameters which can yield large drag reduction while maintaining the stability of SH interfaces in high Reynolds number turbulent flows have been identified.

REFERENCES

ALJALLIS, E., SARSHAR, M. A., DATLA, R., SIKKA, V., JONES, A. & CHOI, C. H. 2013 Experimental study of skin friction drag reduction on superhydrophobic flat plates in high Reynolds number boundary layer flow. *Phys. Fluids* **25** (2), 025103.

ARENAS-NAVARRO, I. 2017 Numerical simulations for turbulent drag reduction using liquid infused surfaces. PhD thesis, The University of Texas at Dallas.

BECHERT, D. W., BRUSE, M., HAGE, W., VAN DER HOEVEN, J. G. T. & HOPPE, G. 1997 Experiments on drag-reducing surfaces and their optimization with an adjustable geometry. *J. Fluid Mech.* **338**, 59–87.

BIDKAR, R. A., LEBLANC, L., KULKARNI, A. J., BAHADUR, V., CECCIO, S. L. & PERLIN, M. 2014 Skin-friction drag reduction in the turbulent regime using random-textured hydrophobic surfaces. *Phys. Fluids* **26** (8), 085108.

CHECCO, A., OCKO, B. M., RAHMAN, A., BLACK, C. T., TASINKEVYCH, M., GIACOMELLO, A. & DIETRICH, S. 2014 Collapse and reversibility of the superhydrophobic state on nanotextured surfaces. *Phys. Rev. Lett.* **112** (21), 216101.

DANIELLO, R. J., WATERHOUSE, N. E. & ROTHSTEIN, J. P. 2009 Drag reduction in turbulent flows over superhydrophobic surfaces. *Phys. Fluids* **21** (8), 085103.

DEAN, R. B. 1978 Reynolds number dependence of skin friction and other bulk flow variables in two-dimensional rectangular duct flow. *Trans. ASME J. Fluids Engng* **100** (2), 215–223.

FU, M. K., ARENAS, I., LEONARDI, S. & HULTMARK, M. 2017 Liquid-infused surfaces as a passive method of turbulent drag reduction. *J. Fluid Mech.* **824**, 688–700.

GARCÍA-MAYORAL, R. & JIMÉNEZ, J. 2012 Scaling of turbulent structures in riblet channels up to $Re_\tau \approx 550$. *Phys. Fluids* **24** (10), 105101.

GOSE, J., GOLOVIN, K., BOBAN, M., MABRY, J., TUTEJA, A., PERLIN, M. & CECCIO, S. 2018 Characterization of superhydrophobic surfaces for drag reduction in turbulent flow. *J. Fluid Mech.* **845**, 560–580.

KARATAY, E., TSAI, P. A. & LAMMERTINK, R. G. H. 2013 Rate of gas absorption on a slippery bubble mattress. *Soft Matt.* **9** (46), 11098–11106.

LAGRAVA, D., MALASPINAS, O., LATT, J. & CHOPARD, B. 2012 Advances in multi-domain lattice Boltzmann grid refinement. *J. Comput. Phys.* **231** (14), 4808–4822.

LING, H., KATZ, J., FU, M. & HULTMARK, M. 2017 Effect of Reynolds number and saturation level on gas diffusion in and out of a superhydrophobic surface. *Phys. Rev. Fluids* **2** (12), 124005.

LING, H., SRINIVASAN, S., GOLOVIN, K., MCKINLEY, G. H., TUTEJA, A. & KATZ, J. 2016 High-resolution velocity measurement in the inner part of turbulent boundary layers over super-hydrophobic surfaces. *J. Fluid Mech.* **801**, 670–703.

MIN, T. & KIM, J. 2004 Effects of hydrophobic surface on skin-friction drag. *Phys. Fluids* **16** (7), L55.

NISHINO, T., MEGURO, T., NAKAMAE, K., MATSUSHITA, M. & UEDA, Y. 1999 The lowest surface free energy based on -CF3 alignment. *Langmuir* **15**, 4321–4323.

PARK, H., PARK, H. & KIM, J. 2013 A numerical study of the effects of superhydrophobic surface on skin-friction drag in turbulent channel flow. *Phys. Fluids* **25** (11), 110815.

PARK, H., SUN, G. & KIM, C.-J. 2014 Superhydrophobic turbulent drag reduction as a function of surface grating parameters. *J. Fluid Mech.* **747**, 722–734.

PHILIP, J. R. 1972 Flows satisfying mixed no-slip and no-shear conditions. *Z. Angew. Math. Phys.* **23** (3), 353–372.

RASTEGARI, A. & AKHAVAN, R. 2015 On the mechanism of turbulent drag reduction with super-hydrophobic surfaces. *J. Fluid Mech.* **773**, R4.

RASTEGARI, A. & AKHAVAN, R. 2018a The common mechanism of turbulent skin-friction drag reduction with super-hydrophobic longitudinal microgrooves and riblets. *J. Fluid Mech.* **838**, 68–104.

RASTEGARI, A. & AKHAVAN, R. 2018b Effect of interface dynamics on drag reduction and sustainability of superhydrophobic and liquid-infused surfaces in turbulent flow. *Bull. Am. Phys. Soc.* **63** (13), 143.

REHOLON, D. & GHAEMI, S. 2018 Plastron morphology and drag of a superhydrophobic surface in turbulent regime. *Phys. Rev. Fluids* **3**, 104003.

ROTHSTEIN, J. P. 2010 Slip on superhydrophobic surfaces. *Annu. Rev. Fluid Mech.* **42**, 89–109.

SAMAHA, M. A., TAFRESHI, H. V. & GAD-EL HAK, M. 2012 Influence of flow on longevity of superhydrophobic coatings. *Langmuir* **28** (25), 9759–9766.

SCHELLENBERGER, F., ENCINAS, N., VOLLMER, D. & BUTT, H.-J. 2016 How water advances on superhydrophobic surfaces. *Phys. Rev. Lett.* **116** (9), 096101.

SCHEWE, G. 1983 On the structure and resolution of wall-pressure fluctuations associated with turbulent boundary-layer flow. *J. Fluid Mech.* **134**, 311–328.

SCHÖNECKER, C., BAIER, T. & HARDT, S. 2014 Influence of the enclosed fluid on the flow over a microstructured surface in the Cassie state. *J. Fluid Mech.* **740**, 168–195.

SEO, J., GARCÍA-MAYORAL, R. & MANI, A. 2015 Pressure fluctuations and interfacial robustness in turbulent flows over superhydrophobic surfaces. *J. Fluid Mech.* **783**, 448–473.

SEO, J. & MANI, A. 2016 On the scaling of the slip velocity in turbulent flows over superhydrophobic surfaces. *Phys. Fluids* **28**, 025110.

SILLERO, J. A., JIMÉNEZ, J. & MOSER, R. D. 2013 One-point statistics for turbulent wall-bounded flows at Reynolds numbers up to $\delta^+ \approx 2000$. *Phys. Fluids* **25** (10), 105102.

SPALART, P. R. & MCLEAN, D. 2011 Drag reduction: enticing turbulence, and then an industry. *Phil. Trans. R. Soc. Lond.* A **369**, 1556–1569.

SRINIVASAN, S., KLEINGARTNER, J. A., GILBERT, J. B., COHEN, R. E., MILNE, A. J. B. & MCKINLEY, G. H. 2015 Sustainable drag reduction in turbulent Taylor–Couette flows by depositing sprayable superhydrophobic surfaces. *Phys. Rev. Lett.* **114** (1), 014501.

SUCCI, S. 2001 *The Lattice Boltzmann Equation: For Fluid Dynamics and Beyond*. Oxford University Press.

TSUJI, Y., FRANSSON, J. H. M., ALFREDSSON, P. H. & JOHANSSON, A. V. 2007 Pressure statistics and their scaling in high-Reynolds-number turbulent boundary layers. *J. Fluid Mech.* **585**, 1–40.

VAN BUREN, T. & SMITS, A. J. 2017 Substantial drag reduction in turbulent flow using liquid-infused surfaces. *J. Fluid Mech.* **827**, 448–456.

WEXLER, J. S., JACOBI, I. & STONE, H. A. 2015 Shear-driven failure of liquid-infused surfaces. *Phys. Rev. Lett.* **114** (16), 168301.

YBERT, C., BARENTIN, C., COTTIN-BIZONNE, C., JOSEPH, P. & BOCQUET, L. 2007 Achieving large slip with superhydrophobic surfaces: scaling laws for generic geometries. *Phys. Fluids* **19** (12), 123601.

ZANOUN, E.-S., NAGIB, H. & DURST, F. 2009 Refined c_f relation for turbulent channels and consequences for high-re experiments. *Fluid Dyn. Res.* **41** (2), 021405.

ZHANG, J., TIAN, H., YAO, Z., HAO, P. & JIANG, N. 2015 Mechanisms of drag reduction of superhydrophobic surfaces in a turbulent boundary layer flow. *Exp. Fluids* **56** (9), 179.

ZHENG, Q.-S., YU, Y. & ZHAO, Z.-H. 2005 Effects of hydraulic pressure on the stability and transition of wetting modes of superhydrophobic surfaces. *Langmuir* **21** (26), 12207–12212.